Renewable Energy 50 (2013) 994–1004

Contents lists available at SciVerse ScienceDirect

Renewable Energy

journal homepage: www.elsevier.com/locate/renene

Numerical simulation of a new type of cross flow tidal turbine using OpenFOAM – Part I: Calibration of energy extraction

Mulualem G. Gebreslassie*, Gavin R. Tabor, Michael R. Belmont

College of Engineering, Mathematics and Physical Sciences, University of Exeter, North Park Road, Exeter EX4 4QF, United Kingdom

ARTICLE INFO

Article history:
Received 10 April 2012
Accepted 17 August 2012
Available online

Keywords:
MRL
Tidal
Power
Extraction
IBF model
LES

ABSTRACT

This paper introduces a new CFD based *Immersed Body Force* (IBF) model, and examines the performance of a new type of tidal turbine, the Momentum Reversal Lift (MRL) turbine, developed by Aquascientific Ltd using the open source computational fluid dynamics (CFD) code OpenFOAM. The IBF model was added as a forcing function into the existing large eddy simulation model to create a momentum change in the fluid flow induced by the MRL turbine. An experimental study was performed on a small scale model to determine the operating efficiency of the turbine and the data was used to validate the IBF model.

The power output curves from both the IBF model and the experiments showed good agreement in most of the data except for a few discrepancies at higher torques, due to venturi flow created by the proximity of the computational domain's wall boundary to the turbine. Thus the results presented in this paper show the fidelity of the IBF model and can be used for different tidal turbine numerical modelling.

1. Introduction

In recent years, interest in exploiting tidal energy using tidal stream devices has been growing rapidly and several studies have been carried out on evaluating the environmental impacts and locating the potential sites as documented by [1–3]. A wide range of tidal stream device designs are currently under development, as well as testing with the aim of improving the efficiency of conventional tidal devices.

Aquascientific Ltd has designed a new type of tidal turbine, Momentum Reversal Lift (MRL) turbine, which is currently in the prototype and testing phase. The MRL turbine is a development of cycloidal turbines and as such has a system of three symmetrical blades which revolve through 180° for every full rotation of the main shaft. This clearly induces very complex, highly sheared internal flows plus a large circulation flows. Experimental studies have been performed on small scale models to determine the operating efficiency of the turbine in a fluid test tunnel. However, it is expensive to perform experimental works to study the device parameters in a large scale and or arrays. Therefore, it is crucial to utilize other options such as numerical simulations which are potentially less expensive.

Numerical models have showed great success in the study of tidal turbines, such as the MRL turbine, though there are still issues to resolve. Detailed modelling of such a system with complex internal motions is a good candidate for overset meshing and/or sliding mesh methods. However, the computational cost of these methods is high. Given that the long term goal is farm scale array modelling such methods are not realistic, hence this study aimed at developing moderate computational cost techniques that have acceptable fidelity.

Alternative numerical models such as the actuator disc method are considerably cheaper to compute, but fail to resolve sufficient detail of the large scale transient flow. The actuator disc method has no capability of resolving the flow around each blade as described by [4]. The aim of this study is therefore to develop a simplified CFD based, *Immersed Body Force* (IBF) model, which is a compromise between at one extreme a full treatment of the internal blade motions and on the other, a highly simplified momentum extraction zone techniques such as the actuator disc method.

2. Methodology

2.1. Experimental study

An experimental study has been undertaken to determine the loading characteristics of the turbine. The model device is shown in Fig. 1. The primary aim of the work was to establish the turbine

* Corresponding author. Tel.: +44 7550747812.
E-mail addresses: mgg204@ex.ac.uk, mulualemtalk@gmail.com (M.G. Gebreslassie).

0960-1481/$ – see front matter © 2012 Elsevier Ltd. All rights reserved.
http://dx.doi.org/10.1016/j.renene.2012.08.065

Nomenclature

A	projected area of turbine (m^2)
C_p	power coefficient
C_T	thrust coefficient
D	turbine diameter (m)
L	length of turbine (m)
ρ	density (kg/m^3)
δ	boundary layer thickness (m)
p	pressure (N/m^2)
ρ_f	water density (kg/m^3)
ρ_g	air density (kg/m^3)
μ	dynamic viscosity (kg/ms)
μ_f	dynamic viscosity of water (kg/ms)
μ_g	dynamic viscosity of air (kg/ms)
F_b	forcing function (N)
F_D	drag force (N)
F_L	lift force (N)
F_s	surface tension (N)
ω	rate of rotation (s^{-1})
τ	torque (Nm)
P	available power from the stream flow (W)
P_{ext}	extracted power (W)
u	stream velocity (m/s)
u_t	averaged velocity through the turbine (m/s)
u_r	averaged blade velocity (m/s)
a	axial induction factor
g	gravitational acceleration (m/s^2)
α	volume fraction of air and water

efficiency under a range of operating conditions and to investigate the optimum configurations.

A water flow tunnel was used for the experimental study of the MRL turbine where the flow was provided using a water pump as shown in Fig. 2. The tests consisted of measurements of flow rates and the rate of turbine rotation under a range of mechanical torque conditions. The flow rate was varied using a controlled water pump and measured using a Rotameter.

The torque output of the turbine was estimated from the forces recorded using a belt and pulley system. The pulley was rigidly attached using grub-screws to the central axis of the turbine. A belt was then wrapped around half of the pulley, with one free end being connected directly to a force meter, and the other free end being connected to a force meter via a small spring, designed to ensure that the belt was held tight against the pulley over a wide range of tensions. As the turbine and hence the pulley rotated, the force was recorded from which the torque was calculated using the known radius of the pulley. Several controlled torques were applied by differential forces on a bobbin of known radius and for a given flow rate in order to obtain the efficiency of the turbine at different torques.

The rate of turbine rotation was measured using a light-gate connected to a data recorder. A disc with 32 holes was connected to the turbine central axis, and as this disc rotated the light-gate recorded the number of holes that passed through its beam, displaying the results as a frequency with units (holes per minute).

The power output of the turbine was estimated using the measured torques and rate of turbine rotation, which can be defined as:

$$P_{ext} = \tau\omega \tag{1}$$

From which the power coefficient can be calculated as the ratio of the power extracted to the available energy of the stream flow as:

$$C_p = \frac{P_{ext}}{\frac{1}{2}\rho A u^3} \tag{2}$$

where, A is the projected area within which flow is directed through the turbine and which represents the maximum swept area of all blades during one complete or multiple cycles. In the case of a horizontal conventional horizontal aerofoil turbine typified by wind turbines, $A = \pi R^2$ where R is the blade radius. In the MRL turbine case, $A = DL$ where D is the diameter and L is the length of the turbine. The area is not represented by a single blade but similarly by the total area swept out around the central axis. This is a function of the specific design and includes the blade width and separation of blades from the central axis. Since the blade is face on at one side of the cycle and edge on at the other side, the cross-sectional area is not symmetric about the central rotation axis.

The uniformity of the flows was first measured across and along the tunnel. The velocity profile at different sections across the tunnel showed fairly uniform velocity except near the walls where the velocities were lower due to the boundary layer interaction with the walls. The results of this experimental study are given in Section 3.1.

2.2. Computational modelling

Most engineering applications including tidal turbines involve turbulent motions. Experiments have been used to study these

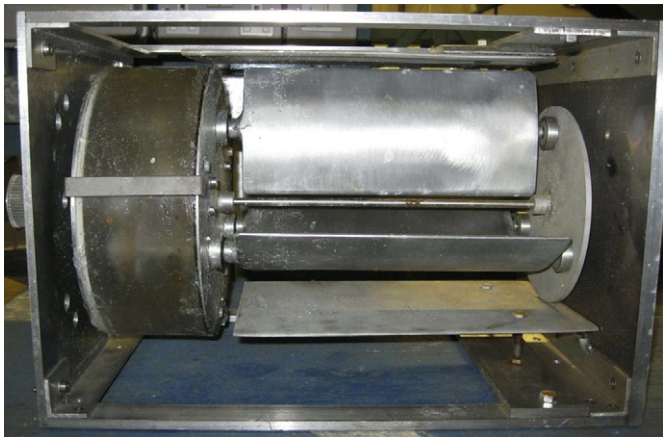

Fig. 1. MRL turbine.

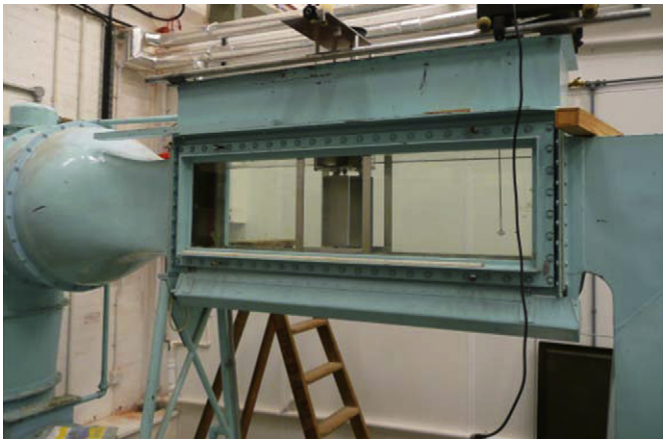

Fig. 2. Experimental set up of the MRL turbine.

turbulent motions for many years, but as engineering devices get increasingly sophisticated, level of detail and accuracy also increase, inflicting massive computational cost and time constraints [5]. Therefore, to minimise the cost and time of experiments, other options have been developed in particular the numerical methods have been introduced and these methods have become more popular and cost effective in optimising sophisticated devices. The most commonly used numerical methods are direct numerical simulation (DNS), large eddy simulation (LES), and Reynolds averaged Navier–Stokes (RANS).

DNS is the most accurate approach for turbulence simulations because of its capability to solve the NS equations by resolving all the motions without averaging or approximations [5]. However, DNS needs very fine meshing to resolve the small scale motions making it extremely computationally expensive. Therefore, turbulence modelling has been extensively developed to get the balance between the computational cost and the satisfaction of the engineering solutions for the descriptions of turbulent motion. The most popular and often utilized models in the simulation of turbulent motions are RANS and LES, and both models showed success in replacing the DNS.

RANS equations are obtained by statistical averaging of the equations of motion. These averaged equations are not closed (number of unknown variables are greater than the number of equations) and requires the introduction of turbulence models. These turbulence models are used to model all the large and small scale motions and depend on the average flow quantities or modelled approximations.

A set of fairly simple turbulence models can be constructed by utilising the Boussinesq approximation, modelling the effect of the unresolved turbulence as a turbulent viscosity (enhancing or replacing the molecular viscosity). The most commonly used turbulence model, the $k-\varepsilon$ model, is of this kind. However, the Boussinesq approximation is an assumption of isotropy in the unresolved turbulence, which is not always appropriate. More sophisticated models include Reynolds stress models, in which algebraic transport models are developed for all independent components of the unresolved (Reynolds) stress term. However, all RANS models suffer for the deficiency that they fail to resolve any of the fluctuating scales in the flow (predominantly although not in practice exclusively stochastic turbulent scales). In cases where the large scale turbulent motions are important it is necessary to employ the alternative, LES methods.

The large scale eddy sizes of a turbulent motion are represented by the LES models and are most energetic, making them the most effective way of transporting the conserved properties [5]. In contrast, the small scale eddy sizes are weaker to transport the conserved properties. Therefore, the LES modelling approach is best suited for the task and resolves the large scale turbulent motions by solving the 3D time dependent NS equations while modelling the small scale motions using sub-grid scale (SGS) methods. The LES was therefore chosen in this study in order to balance the weakness and strength of the DNS and RANS.

2.2.1. LES governing equation

The LES governing equation utilized for the simulation is a combination of the filtered NS equations and source terms as shown in Eq. (4). Additionally, the presence of the free surface interface between the air and water is treated through the commonly used Volume of Fluid (VOF) method, by introducing a volume fraction α and solving an additional modelled transport equation for this quantity [6]. In this study, a new source term, forcing function (F_b), was added to the existing LES model to create a momentum change in the fluid flow by the turbine blades. Both the filtering process and the source terms of the LES governing equations are discussed in the subsequent sections. A detailed explanation about the new source term added in this study to the existing LES equation is also given in Section 2.2.5.

2.2.2. Filtered Navier–Stokes equations

Filtering the NS equations is essential to separate the velocity field that contains the large scale components, which is performed by filtering the velocity field [7]. Using the one-dimensional notation, the filtered velocity is defined as:

$$\overline{u}_i(x) = \int G(x,x')u_i(x')\mathrm{d}x' \tag{3}$$

Where $G(x,x')$ is the filter kernel, which is a localized function. The eddy sizes are identified using a length scale, Δ. Eddies that are larger than Δ are roughly considered as large eddies, the ones that are resolved. These which are smaller than Δ are small eddies.

The filtered NS equations for incompressible flow produce a set of equations [8] that can be defined as:

$$\frac{\partial \overline{u}_i}{\partial t} + \frac{\partial}{\partial x_j}\left(\overline{u_i u_j}\right) = -\frac{1}{\rho}\left(\frac{\partial \overline{p}}{\partial x_i} + \delta_{i1}\frac{\partial \langle P\rangle}{\partial x_1}\right) + \nu\frac{\partial}{\partial x_j}\left(\frac{\partial \overline{u}_i}{\partial x_j} + \frac{\partial \overline{u}_j}{\partial x_i}\right) + \rho g + \overline{F}_s + \overline{F}_b \tag{4}$$

But the continuity equation does not change by the filtering process because of its linearity and can be written as:

$$\frac{\partial \overline{u}_i}{\partial x_i} = 0 \tag{5}$$

Where the bar $\overline{(.)}$ is the grid filter operator, $\overline{u}$ is the filtered velocity, $\overline{p}$ is the filtered pressure, ν is a dimensionless kinematic viscosity, δ_{i1} is the Kronecker-delta, and $\frac{\partial\langle P\rangle}{\partial x_1}$ is the driving force which vanishes if periodic inlet-outlet boundary conditions are not applied.

Since $\overline{u_i u_j} \neq \overline{u}_i\overline{u}_j$, the filtered convection term $\overline{u_i u_j}$ is the cause of difficulty in LES modelling because of its non-linearity. Ref. [7] introduced a modelling approximation for the difference of the two inequalities and splits them as:

$$\tau_{ij} = -\overline{u_i u_j} + \overline{u}_i\overline{u}_j \tag{6}$$

Where the new linking term τ_{ij} is the SGS Reynolds stress. Combining Eqs. (4) and (6), the filtered NS equations can be rewritten as:

$$\frac{\partial \overline{u}_i}{\partial t} + \frac{\partial}{\partial x_j}\left(\overline{u}_i\overline{u}_j\right) = -\frac{1}{\rho}\left(\frac{\partial \overline{p}}{\partial x_i} + \delta_{i1}\frac{\partial \langle P\rangle}{\partial x_1}\right) + 2\nu\frac{\partial}{\partial x_j}\overline{S}_{ij} - \frac{\partial \tau_{ij}}{\partial x_j} + \rho g + \overline{F}_s + \overline{F}_b \tag{7}$$

where $\overline{S}_{ij}$ is the strain rate of the large scales or resolved scales and is defined as:

$$\overline{S}_{ij} = \frac{1}{2}\left(\frac{\partial \overline{u}_i}{\partial x_j} + \frac{\partial \overline{u}_j}{\partial x_i}\right) \tag{8}$$

The SGS Reynolds stress has to be approximated by using SGS models to get a full solution for the NS equations.

2.2.3. Sub-grid scale models

The resulting SGS Reynolds stresses from the filtering processes are unknown and need modelling. The stresses are a large scale momentum flux resulting from the unresolved scales. Most of the time, these stresses have been approximated by SGS models developed based on the eddy viscosity. The most popular SGS models extensively used for simulations include One-equation eddy viscosity, Smagorinsky, the kinetic-energy model and the dynamic model. The Boussinesq hypothesis is commonly employed in the SGS turbulence models [9] and calculates the SGS stress using a linear relationship with the rate of strain tensor.

The earliest SGS model is the Smagorinsky model proposed by [10]. Though the Smagorinsky model has been relatively successful, it has had some problems especially if the flow is highly complex and has shear flows. Several modifications have had to be made in the Smagorinsky model if used for channel flow simulations as described by [5]. Therefore, a better model has to be chosen for the MRL simulations.

The one-equation eddy viscosity model (*oneEqEddy*) developed by [11] has been used in a wide range of turbulent problems and is much better than the Smagorinsky model as described by [12]. Thus, the one-equation model has been used to model the small scale motions in the MRL turbine simulation. Based on the *oneEqEddy* model [11], the sub-grid stresses are defined as:

$$\tau_{ij} = \frac{2}{3}k_S\delta_{ij} - 2\nu_t\left(\overline{S}_{ij} - \overline{S}_{kk}\delta_{ij}\right) \tag{9}$$

where ν_t is the SGS eddy viscosity given as:

$$\nu_t = C_k\overline{\Delta}\sqrt{k_S} \tag{10}$$

and the sub-grid kinetic energy k_S is given as:

$$k_S = \frac{1}{2}\left(\overline{u_k u_k} - \overline{u}_k\overline{u}_k\right) \tag{11}$$

where: $C_k \sim 0.4$

2.2.4. Volume of fluid method (VOF)

The MRL turbine is designed to operate relatively close to the water surface and the dynamics of the free surface will be important for the overall behaviour of the turbine. The VOF method has been widely used in the study of floating body applications, breaking waves, non linear free surface flows and other multiphase flows to handle these kinds of problems, as documented by [13–16]. It is an easy, flexible and efficient method for treating free boundaries as described by [17] and was used in this study coupled with the LES model.

The volume of water in a cell is calculated as $F_{\text{vol}} = \alpha V_{\text{cell}}$, where V_{cell} is the volume of a computational cell and α is the water fraction of a cell. If the cell is completely filled with fluid then $\alpha = 1$ and if it is void then its value should be 0. The interface between the phases is represented by values of α between 0 and 1.

The value of α is calculated from a separate transport equation as

$$\frac{\partial\alpha}{\partial t} + \nabla\cdot(\alpha\overline{u}) = 0 \tag{12}$$

During the simulations, there is a surface compression and in OpenFOAM, an extra artificial compression term which is active only on the interface region is introduced into Eq. (12) as follows:

$$\frac{\partial\alpha}{\partial t} + \nabla\cdot(\alpha\overline{u}) + \nabla\cdot(\alpha(1-\alpha)u_c) = 0 \tag{13}$$

Where: u_c is a velocity field suitable to compress the interface. The physical properties (μ and ρ) at any point in the domain are calculated as a weighted averaged of the volume fraction of the two fluids, α, as:

$$\mu = \alpha\mu_f + (1-\alpha)\mu_g \tag{14}$$

$$\rho = \alpha\rho_f + (1-\alpha)\rho_g \tag{15}$$

2.2.5. Turbine modelling

The principle of actuator disc has been frequently utilized for modelling turbines both in experiments and computational studies. The disc acts as a momentum sink reducing the flow momentum which is matched to the thrust coefficients of the turbine [4]. The pressure drop, Δp, is imposed as a source term into the NS equations creating a pressure drop across the disc through Darcy's Law with an additional inertial loss term.

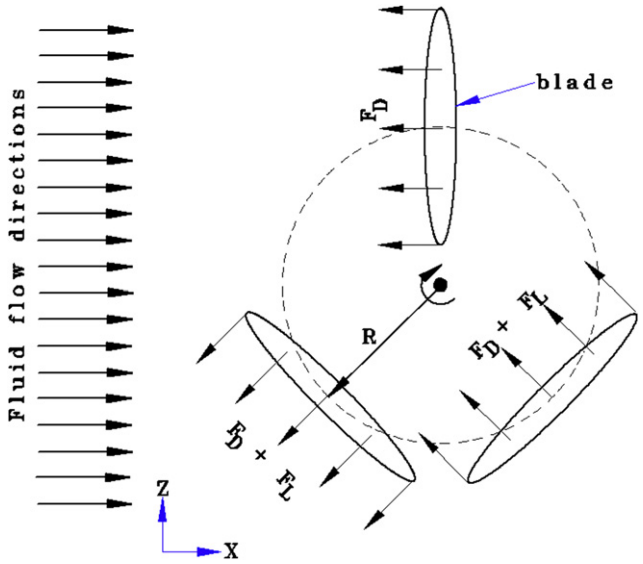

Fig. 3. Schematic representation of the force directions of the *blade* method IBF model.

Several studies were performed by [4,18–20] using the actuator disc method for the simulation of tidal turbines. Studies by [4,19,21] indicated that the actuator disc method minimizes the requirement of mesh refinement and modelling the geometry in full, reducing the associated computational costs and has shown good agreement with experimental data but [19] acknowledged that the vortex shedding from the edge of the disc was not similar with rotating blades and lacks swirl producing flow. The study by [4] also indicated that the actuator disc method has no capability of resolving the flow around each blade except reducing the momentum of the fluid as it passes through the disc.

Understanding the effect of blade rotation is crucial in the study of tidal turbines to correctly describe the free surfaces and the downstream wake characteristics which is the main concern of using the actuator disc method. In this study, a new tidal turbine

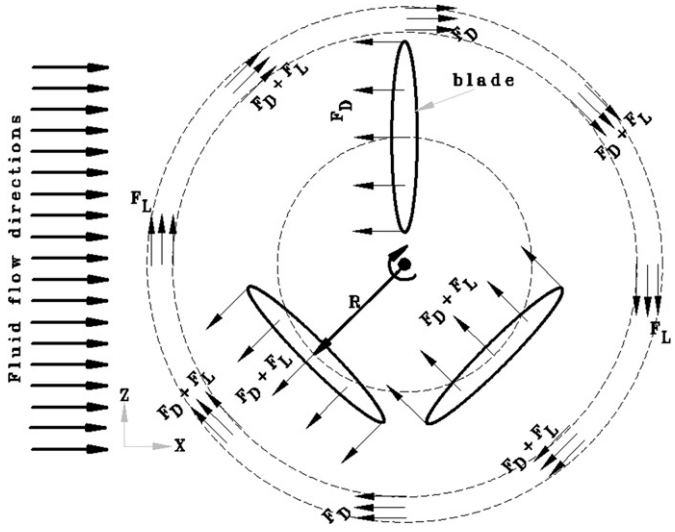

Fig. 4. Schematic representation of the force directions of the *annular* method IBF model.

modelling method called *Immersed Body Force* (IBF) is therefore introduced. For the IBF approach, a forcing function (F_b) is used representing the force applied by the immersed body (turbine) to the fluid to create momentum change and rotational flows. The forcing function can be defined as:

$$\overline{F}_b = \overline{F}_D + \overline{F}_L \tag{16}$$

The forcing function was added in the NS equations and a code was developed by considering drag and lift forces applied by the blades on the fluid flow as shown in Fig. 3. The IBF approach has the capability of producing complex internal flows similar to the realistic bladed turbine flows compared with the actuator disc method.

The body force is implemented uniformly throughout the volume of the blades and is assumed to be constant as shown in Fig. 3. The force applied by the top blade to the approaching fluid flow was considered entirely as a drag force while the force applied by the other two blades have both drag and lift forces. The way the body forces are applied in Fig. 3 was slightly modified in the second approach by introducing additional body forces on the annular section as shown in Fig. 4. The additional forces help in order to induce a circulation flow which represents the rotation of the whole turbine (shaft rotation) relative to the blades. The models described in Figs. 3 and 4 are denoted *blade* and *annular* methods respectively for subsequent discussions.

This IBF method is a compromise between at one extreme a full treatment using overset meshing and/or sliding mesh techniques to describe the detailed internal blade motions and at the other a highly simplified momentum extraction zone such as the actuator disc method.

2.2.6. Data analysis

The power taken off by the turbine was estimated using the power coefficient (C_P) defined by the simple one-dimensional momentum theory as [22]:

$$C_p = 4a(1-a)^2 \tag{17}$$

and the thrust coefficient (C_T) is defined as:

$$C_T = 4a(1-a) \tag{18}$$

where: a is axial induction factor defined as $a = (1-(u_t/u))$. From Eq. (17), it is easy to show that the maximum power coefficient occurs when $a = 1/3$. The power output was calculated using the stream velocity and the power coefficient as:

$$P_{\text{ext}} = C_P \frac{1}{2}\rho A u^3 \tag{19}$$

2.3. Computational domain and boundary conditions

2.3.1. Computational domain set up

Fig. 5 shows a schematic representation of the three dimensional geometry that was used for the computation. It was designed to replicate the uniform flow conditions in the test tunnel. The small scale dimension of the tidal turbine shown in Fig. 1 was represented by the IBF model in the centre of the computational domain. The dimensions of the domain were matched with the fluid test tunnel used for the experimental work to account any blockage effects that can occur.

The initial condition of the whole domain was occupied with two phase fluid, water and air, as shown in Fig. 5 separated by the free surface line before the computation starts. The water level was at 1.5D from the ground floor with the rest of the domain occupied by air.

The domain size was 3.625D upstream and downstream of the turbine with the width and overall height being 3D and 2.5D respectively. The aspect ratio of the turbine prototype is 1.1. The turbine has an overall diameter of $D = 0.20$ m and a length of $L = 0.22$ m. The blades have maximum thickness and height of 1.7 cm and 9.5 cm respectively. The spacing between the turbine and the wall boundary on both sides is 1D. The spacings between the turbine with the bottom wall boundary and the free surface are 2.5D and 0.15D respectively.

Fig. 6a shows the blades at a fixed position which were used for the simulation purposes. Fig. 6b shows the force directions which represent the forcing function (IBF model). One of the blades was vertical and the other two at an angle, acting as a jet and lift blade respectively.

The number of cells used in the computational domain are listed in Table 1 where the cell count in the horizontal and vertical directions were represented by N_x and N_y respectively and along the span of the domain by N_z. Different cell sizes were used in order to reduce the computational cost. The cell sizes were refined in the zone of interest around the turbine region, in order to create a uniform computation, as shown in Fig. 7.

2.3.2. Implementation of boundary condition

The computational domain contains seven boundary patches, namely *atmosphere*, *seaBed*, *wall*, water and air inlet and outlet. The

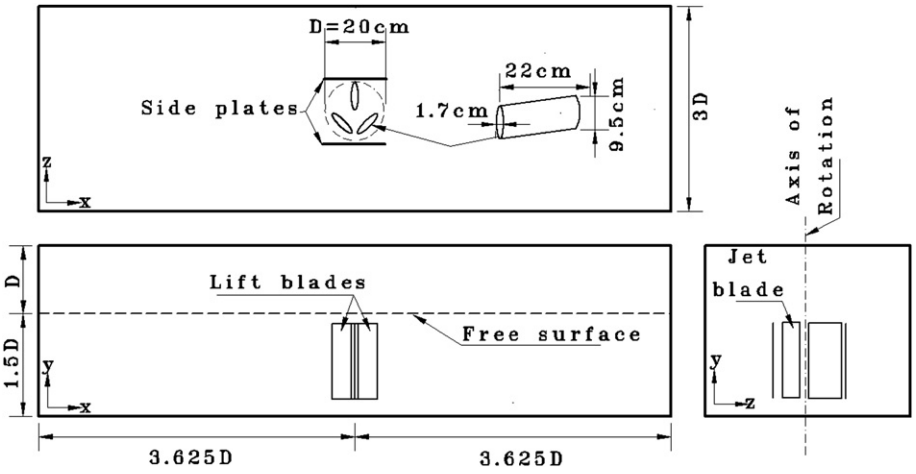

Fig. 5. Computational domain geometry.

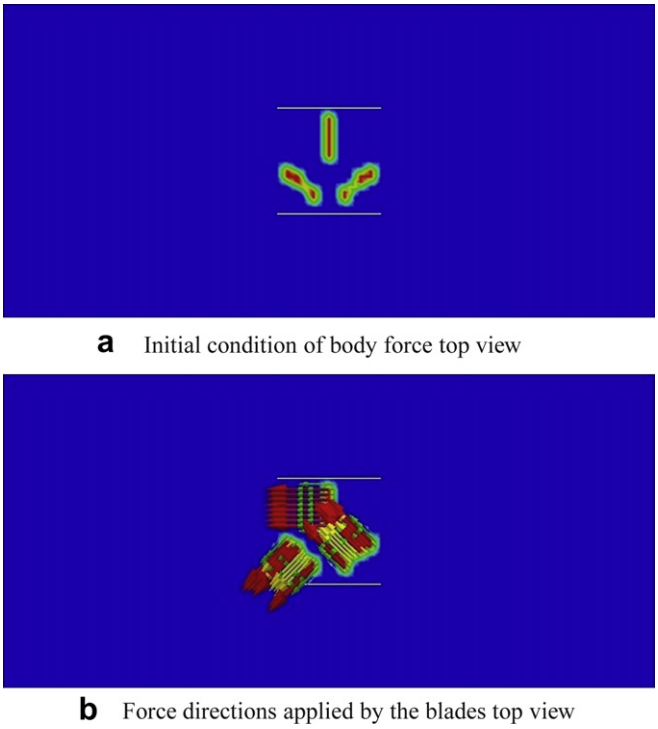

Fig. 6. Snapshots of blade positions and force directions applied by each of the blade.

top part of the domain was an atmosphere which represents a standard patch. This top boundary was free to the atmosphere and allows both outflow and inflow according to the internal flow. This was developed by a combination of pressure and velocity boundary conditions [6].

seaBed and *wall* are the floor and the front and back side of the computational domain respectively and both patches represent a wall. A *zero gradient* boundary condition was applied to the pressure field.

Practically the velocity profile is different across the depth of a channel as discussed in the second paper. However, the experimental study has been carried out in a tunnel where the velocity profile was nearly uniform as discussed in Section 2.1. Therefore, a constant velocity field was applied at the *Inlet*, which represents the patch where the water phase enters in to the domain, to avoid any differences in the comparison of the experiments and the IBF model results.

The boundary layer thickness (δ) grows with distance from the inlet to the outlet, which is difficult to put the exact size of the boundary layer of the whole computational domain. However, the size of the boundary layer at a given distance can be easily obtained and this thickness at the outlet of the domain is 0.65D.

3. Results and discussions

3.1. Experiments

Fig. 8 shows the torque output of the device against the averaged blade velocity for 4 different flow rates. The device generated a maximum torque of 0.76 Nm at a flow rate of 0.875 m/s. The generated torque was increased with an increased flow rate and showed the device's ability to operate in water with a wide range of flow rates which would be encountered in any tidal stream situation.

Table 1
Number of cells used for the computational domain.

Coordinate	Number of cells
X-axis(N_x)	50
Y-axis(N_y)	24
Z-axis(N_z)	42
Total	50,400

The results showed that there is strong negative correlation with a nearly linear relationship in which the device slows with an increased torque output.

A peak power of 5.5 W was generated at a flow rate of 0.875 m/s as shown in Fig. 9. The power curve showed the significance of the range of mechanical torques on the power output. As the turbine rotational speed increased, this results in a falling value of the relative velocity ($u-u_r$), the power output increased to a peak and falls back to a lower value. These measurements demonstrate the cubic dependence of the power on flow velocity as expected.

The power coefficient peaks at a measured velocity ratio of about 0.5 as shown in Fig. 10. This shows that the MRL model can extract maximum energy from the flow when it is rotating at a rate that gives its blades a tangential velocity close to 0.5 of the flow rate. It was clear from the results that the maximum power coefficient occurred at the same velocity ratio for most of the flow rates tested.

3.2. IBF model results

The experimental studies were carried out with the MRL turbine in a vertical axis though the device is designed to operate in a horizontal axis configuration. The aim of the experiment was to obtain the operating conditions of the turbine.

Therefore, two configurations were used for the IBF model simulations. First with a vertical axis configuration with the intention to compare the results with the experimental data, and the second was simulated with a horizontal axis, by increasing the width of the computational domain, to investigate the performance of the turbine when it operates in its intended operating configuration. In the first configuration the *blade* method was used whereas, in the second configuration both the *blade* and *annular* methods were used to make comparisons between them. Three flow rates measured during the experimental study were used for the simulation of the MRL turbine using the IBF model. In the vertical axis configuration simulations, two of the flow rates (0.875 m/s and 0.808 m/s) were used while in the horizontal axis configuration, 0.875 m/s and 0.746 m/s were used. Most of the data used in the analysis were time averaged during the simulations as these data are more realistic than instantaneous data because instantaneous values define a condition at a specified time step, which may have some effect on the results.

3.2.1. Vertical axis

The momentum of the flow was reduced as it passed through the absorption zone created by the presence of the immersed body forces as shown in Fig. 11. However, the velocity contour clearly shows the magnitude of the impact of different values of body forces on the momentum change. The momentum absorption zone was set within the dotted region between the side plates as shown in Fig. 11a for all the simulations.

Fig. 11b shows large reduction of momentum in the downstream flow compared with Fig. 11a, which was caused by the maximum torque (0.76 Nm). The effect of the different torque values can be observed in terms of the averaged velocity magnitude through the turbine as shown in Fig. 12. The velocity and torque showed

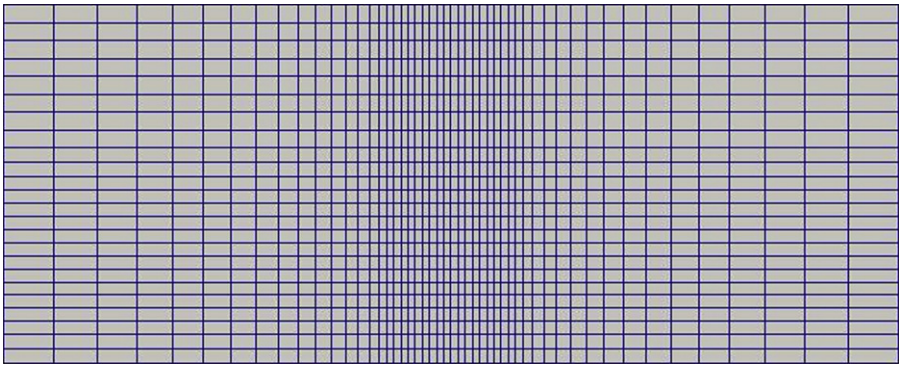

Fig. 7. Non uniform mesh representation of the domain.

a negative correlation similar to the experiments by which the velocity was decreased as the torque increased, which has a direct relation with the change in momentum.

The flow along the centreline of the turbine was affected, compared with the initial stream flow, as shown in Fig. 13. The flow was decreased as it passed through the momentum absorption zone and starts to recover back further downstream, though the domain used was not enough for full recovery.

Fig. 14 shows the instantaneous pressure gradient line along the centreline of the lift blades. The larger torque ($\tau = 0.76$ Nm) caused high pressure drop across the turbine compared with the smaller torque ($\tau = 0.40Nm$) and gave a higher value at the inlet. Both torques produced high pressure at the inlet compared with the downstream of the turbine due to the blockage effect. The discontinuity observed across the turbine is the effect due to the way the two lift blades were positioned, which was an expected result.

The power output curve is shown in Fig. 15 for the two flow rates (0.875 m/s and 0.808 m/s) tested. As the torque increased, which results in a falling value of u_t, the power output increased to a peak value and decreased at a slower rate. There was an indication from the experimental results that the power curve decreased at a slower rate at higher torques. However, the power curve from the IBF model looks more flat at high torques. This was due to the fact that the averaged velocity through the turbine was decreased at a slower rate at higher torques, as shown in Fig. 12. There are two likely reasons for this result. Firstly, it may be due to a trade-off between the increased blockage of the flow by the immersed body forces and an increased flow rate through the venturi created between the blades. Secondly, the flow has to pass through the bypass between the computational domain's wall boundary and the side plates of the turbine to compensate the blockage by the immersed body forces but due to close proximity of the wall boundary, the flow could still be forced to pass between the blades in higher velocity than expected.

3.2.2. Horizontal axis

The simulations were performed by increasing the width of the computational domain to accommodate the turbine in a horizontal axis configuration. The computational domain dimensions given in Fig. 5 were changed according to Table 2. The diameter of the turbine remains constant. The turbine was submerged at 0.625D from the free surface to the top of the upper side plate.

Fig. 16 shows the velocity contours on a vertical plane across the centre of the turbine at the maximum and minimum torques. In the horizontal axis configuration, the flow was accelerated at the top and bottom of the turbine due to the direction of the applied forces by the blades that divert the flow to pass through these bypass regions, which had adverse effect on the free surface. However, the flow was accelerated on both sides of the turbine in the vertical axis configuration which had minimal effect on the free surface. The horizontal axis configuration is therefore better to investigate the effect of energy extraction to the free surface though it is not within the focus of this paper.

The power output curve decreased at a faster rate at higher torques as shown in Fig. 17 compared with the results from the vertical axis configuration (Fig. 15), where the power output curve decreased at a slower rate after the peak value. This was due to a lower averaged velocity through the turbine measured in the horizontal axis configuration.

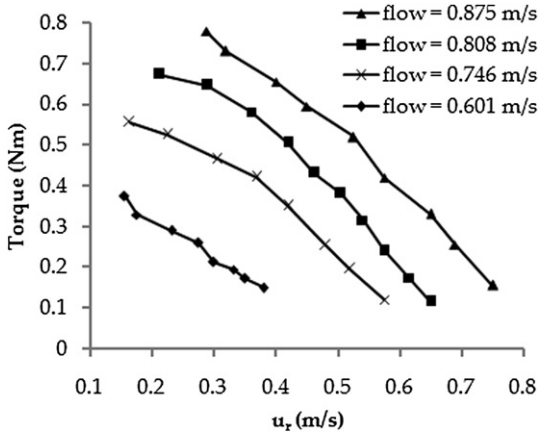

Fig. 8. Torque output vs. averaged blade velocity.

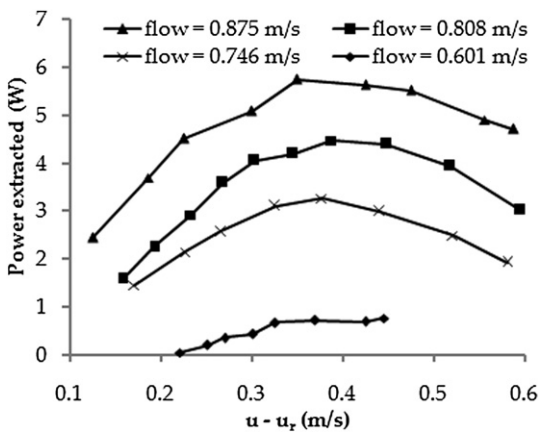

Fig. 9. Power output vs. relative velocity at different flow rates.

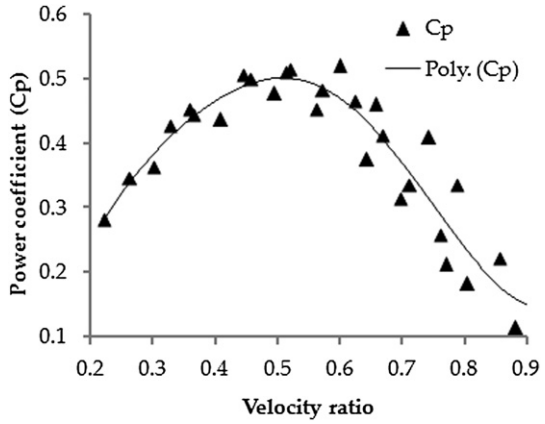

Fig. 10. Power coefficient vs. velocity ratio (u_r/u) at different flow rates.

The likely reason for the better results obtained from the horizontal axis configuration was that the distance between the *seaBed* boundary and the turbine (2.075D) was greater than the proximity of the computational domain's wall boundary to the turbine (1D) in the vertical axis configuration. The interface between the two fluids, water and air, was at a distance of 0.625D from the top of the turbine side plates but its effect was minimal compared with the proximity of the walls. Thus, it is a clear indication that a simulation should be carried out with sufficient space between the wall boundary and turbine to minimize the effect of its interaction.

Fig. 18 shows the power coefficient against the ratio of the turbine to stream velocity (u_t/u). For these particular simulation data, the peak power coefficient occurs at a velocity ratio of 0.75 and 0.66 for the flow velocities of 0.875 m/s and 0.746 m/s respectively. However, it should be noted that there could be a possibility of peak value before and after the given velocity ratios if several simulations were performed, which is time consuming. Thus, using a polynomial fitting curve to the calculated power coefficient data makes it easier to show that the maximum power coefficient occurred at $a = 0.34$ or $(u_t/u) = 0.66$, which is the same

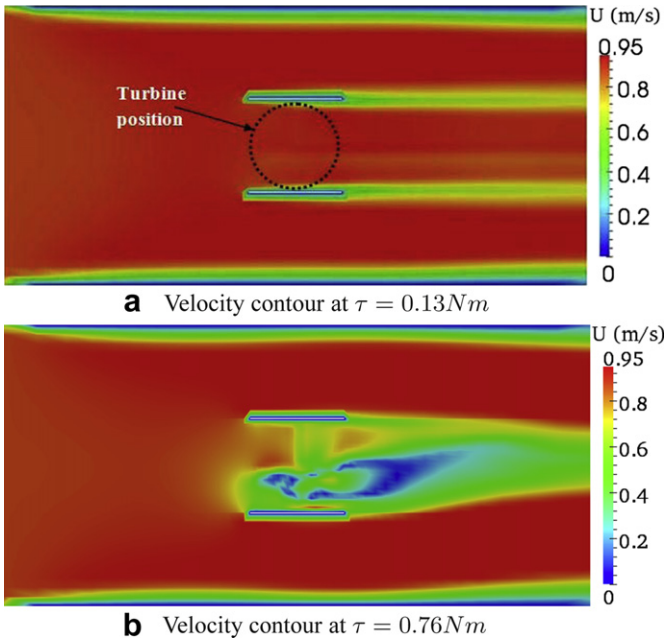

Fig. 11. Velocity contours on horizontal plane across the centre of the turbine simulated using the *blade* method.

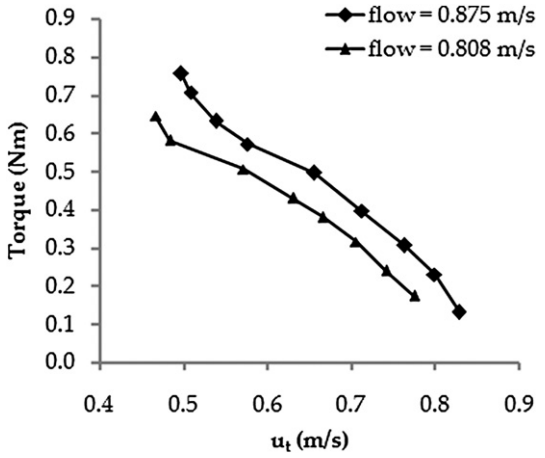

Fig. 12. The effect of torque on the averaged velocity through the turbine.

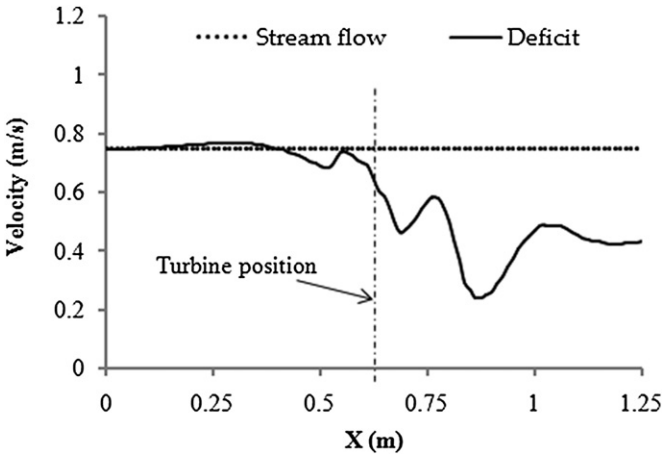

Fig. 13. Velocity deficit at the maximum power extracted for the flow rate of 0.875 m/s.

as the velocity ratio where the peak value occurs for the flow rate of 0.746 m/s. This velocity ratio is close to the theoretical axial induction factor described in Section 2.2.6.

The thrust coefficient against the velocity ratio is given in Fig. 19. The result shows that as the loading increases, the thrust coefficient increases and the velocity ratio decreases as expected.

3.2.3. Comparison of the annular and blade methods of the IBF model

The computational domain used in Section 3.2.2 was utilized for the simulation of the MRL turbine using the *annular* method, and

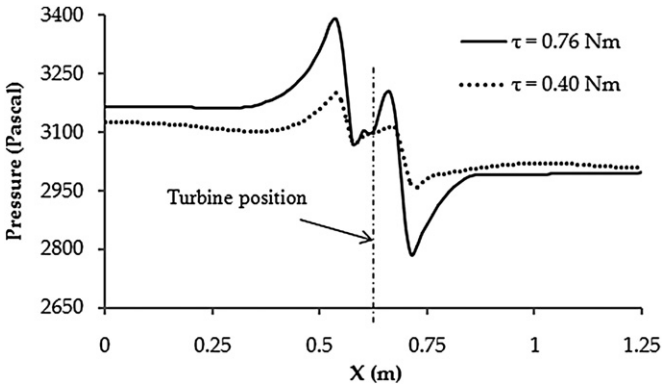

Fig. 14. The effect of torques on the pressure profile for the flow rate of 0.875 m/s.

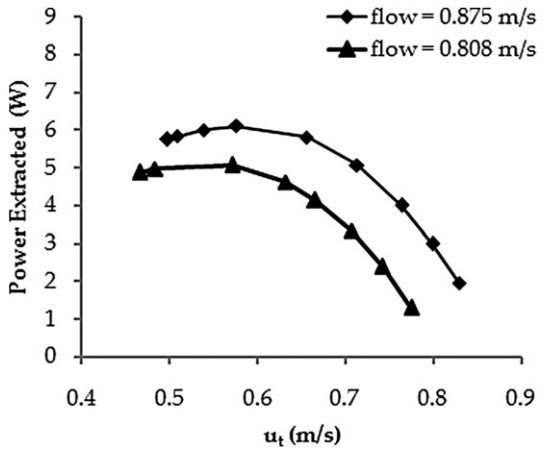

Fig. 15. Power output curve by the vertical axis configuration of the MRL turbine.

Table 2
Computational domain dimension changes.

Label	Original dimension	New dimension
Diameter	$D = 0.2$ m	$D = 0.2$ m
Upstream	3.625D	2.5D
Downstream	3.625D	10D
Width	1.5D	6D
Water level	1.5D	3.75D
Air level	D	1.25D

the results were compared with the *blade* method results of the horizontal axis configuration.

Fig. 20 shows the velocity contours at the minimum and maximum torques. The velocities given in Fig. 20a and Fig. 16a show no difference in both cases because of the small torque which was unable to produce downstream wake. In contrast, Fig. 20b and Fig. 16b showed large scale vortexes downstream of the turbine due to the maximum torques applied.

The power output curves from the two methods showed good agreement as shown in Fig. 21 except for a small difference at higher torques for the flow rate of 0.875 m/s (Fig. 21a).

The similarity of the power output curve from the two methods of the IBF model means that there is no problem to use either of them to estimate the performance of the device. However, it is important

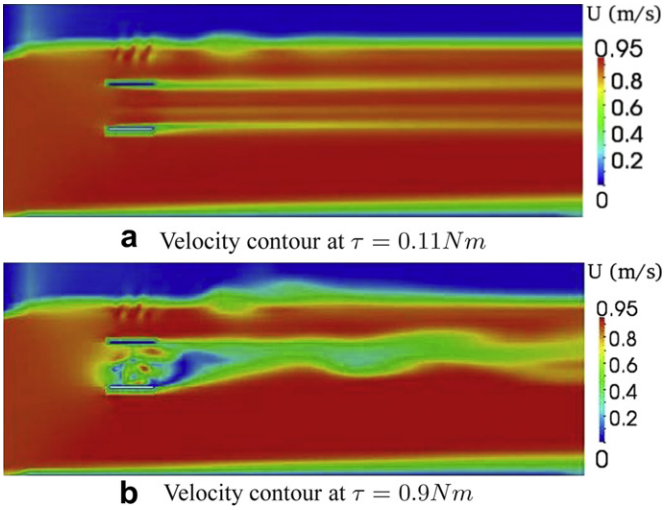

Fig. 16. Velocity contours on the vertical plane across the centre of the turbine simulated using the *blade* method.

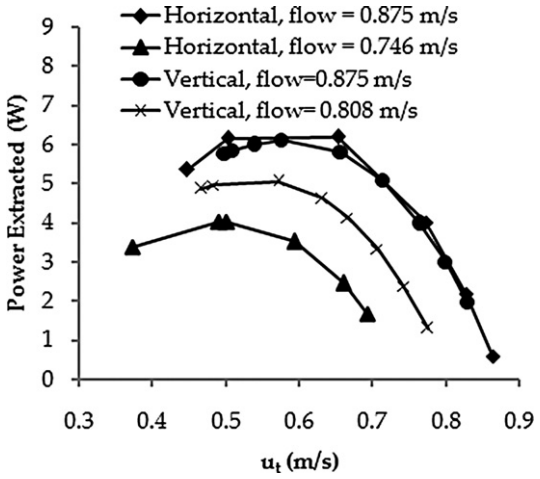

Fig. 17. Comparison of the power output curve by the horizontal and vertical axis configuration of the MRL turbine.

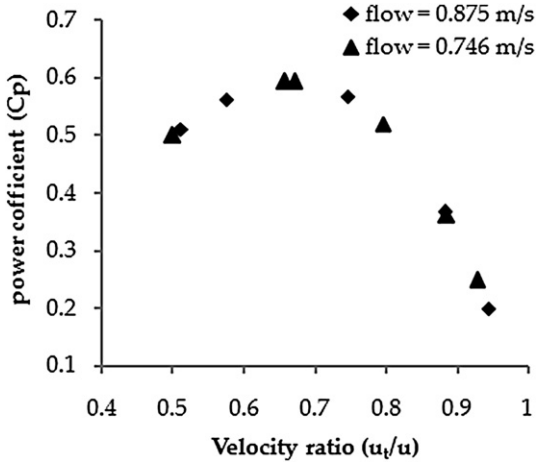

Fig. 18. Power coefficient vs. velocity ratio.

to consider other parameters which need to be investigated to understand the power extraction effects such as the downstream wake and turbulent structures, turbine to turbine interactions, swirling flows, and free surfaces. The velocity contour from the *annular* method at the maximum torque (Fig. 20b) showed high

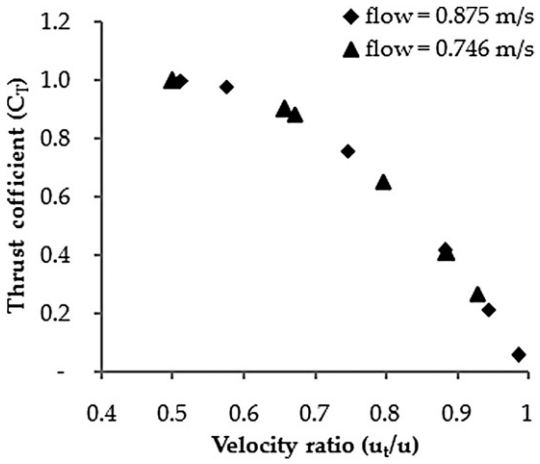

Fig. 19. Thrust coefficient vs. velocity ratio.

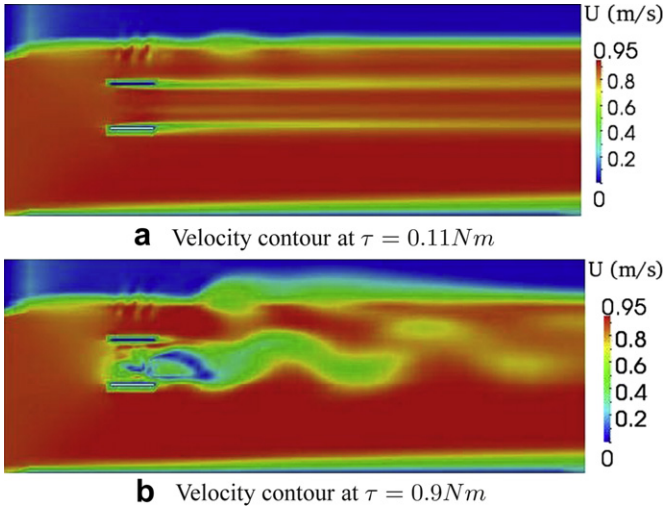

Fig. 20. Velocity contours on a vertical plane across the centre of the turbine simulated using the *annular* method.

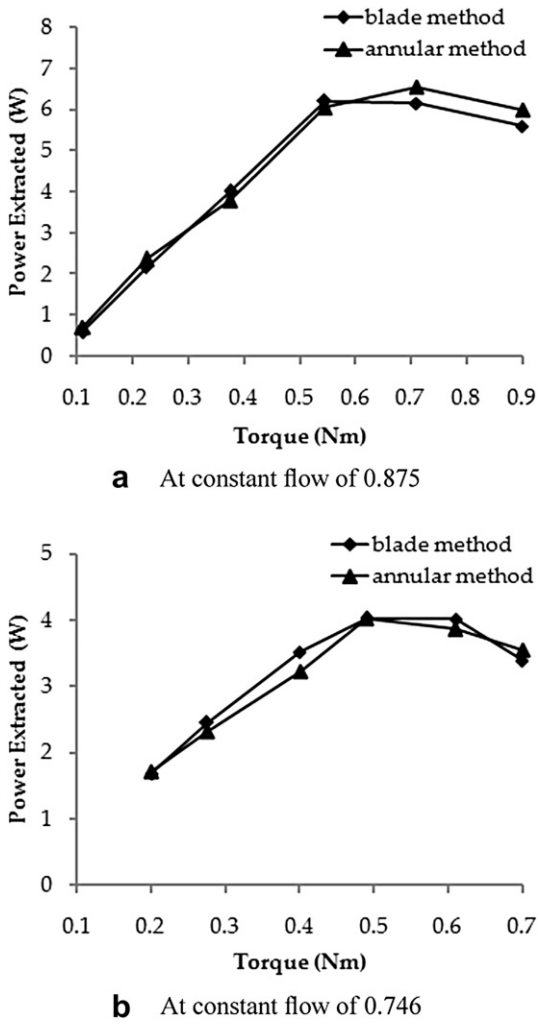

Fig. 21. Power extracted at different applied torques using the alternative turbine modelling for horizontal axis.

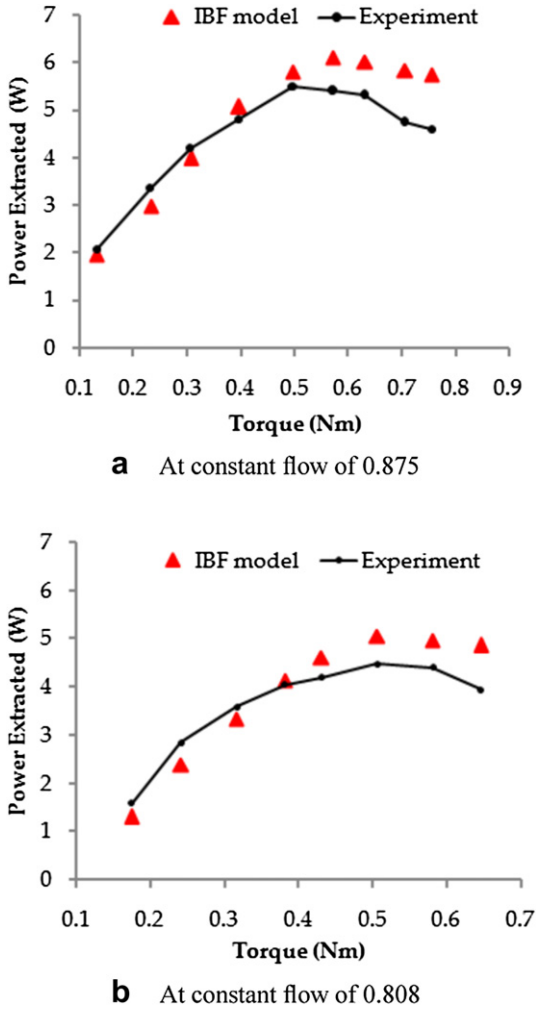

Fig. 22. Power output curve of the experimental and IBF model.

turbulent structures and recovers faster compared with Fig. 16b. In addition, the body forces imposed on the *annular* section of the turbine induce swirling flows similar to those that the real turbines create. A combination of these advantages make the *annular* method a better choice for further studies especially in the investigation of turbine to turbine interaction problems in a tidal stream farm.

3.3. Comparison of the IBF model and experimental results

The experimental results (Section 3.1) and the IBF model results (Section 3.2.1) were used for the comparison using a sample of two flow rates (0.875 m/s and 0.808 m/s). The operating conditions of the experiments and the IBF model were similar to minimise any differences which may occur on the results.

Fig. 22 shows the IBF model and experimental results of power output. The power curve of the IBF model showed good agreement with the experimental results at lower torques (before the peak value) though the IBF model results appear to be a bit lower. The side plates created a venturi flow which dominates the effect of the immersed body forces by which the measured averaged velocity through the turbine was increased than expected that led to a lower power output.

In contrast, the IBF model generated higher power at high torques mainly after the peak power of the experimental results (see Section 3.2.1 for a detailed discussion of the main reasons for this high power output).

If the experiments were carried out with a horizontal axis configuration, the results might show better agreement because the IBF model results simulated in a horizontal axis showed lower power output at higher torques than the vertical axis as discussed in Section 3.2.2. However, some differences would be expected due to the assumptions made for the IBF model and the effects that could occur from the experimental study carried out in a constrained environment, but the magnitude of their difference is reasonable and acceptable.

4. Conclusion

The IBF model results were affected by the proximity of the computational domain's wall boundary and the turbine which led to higher power output at higher torques in the vertical axis configuration. The result was improved when the MRL turbine was simulated in a horizontal axis configuration because of minimal interaction between the wall boundary and the turbine. This was an indication that the IBF model needs sufficient separation between the wall boundary and the device to minimize these effects.

Despite these small differences, the IBF model results showed reasonable agreement with the experimental data, which demonstrates the feasibility of the IBF model developed and can therefore be used for different tidal stream device simulations.

Acknowledgement

One of the authors would like to thank for the financial assistance received from University of Exeter for this study.

References

[1] Bedard R, Previsic M, Siddiqui O, Hagerman G, Robinson M. Survey and characterization tidal in stream energy conversion (TISEC) devices. EPRI Final Report, EPRI-TP-004 NA; 2005.
[2] Hagerman G, Polagye B, Bedard C, Previsic M. Methodology for estimating tidal current energy resources and power production by tidal in-stream energy conversion (TISEC) devices; 2006.
[3] Andrew, B. Phase II tidal stream energy assessment. Tech. Rep.; Technical report 107799/D/2200/03, Black and veatch ltd on behalf of carbon trust; 2005.
[4] Gant S, Stallard T. Modelling a tidal turbine in unsteady flow. In: Proceedings of the eighteenth (2008) international offshore and polar engineering conference. 2008, p. 473–79.
[5] Ferziger J, Perić M. Computational methods for fluid dynamics, vol. 2. Berlin: Springer; 1999.
[6] Ltd O. User guide, http://www.openfoam.com/docs/user/; 2011.
[7] Leonard A. Energy cascade in large-eddy simulations of turbulent fluid flows. Advances in Geophysics 1974;18:237–48.
[8] Xie Z, Castro I. LES and RANS for turbulent flow over arrays of wall-mounted obstacles. Flow, Turbulence and Combustion 2006;76(3):291–312.
[9] Boussinesq J. Théorie de l'écoulement tourbillant (theories of swirling flow). mém prés par div savants à l'acad Sci Paris 1877:23.
[10] Smagorinsky J. General circulation experiments with the primitive equations. Monthly Weather Review 1963;91(3):99–164.
[11] Yoshizawa A, Horiuti K. A statistically-derived subgrid-scale kinetic energy model for the large-eddy simulation of turbulent flows. Journal of the Physical Society of Japan 1985;54(8):2834–9.
[12] Menon S, Yeung P, Kim W. Effect of subgrid models on the computed inter-scale energy transfer in isotropic turbulence. Computers & Fluids 1996;25(2):165–80.
[13] Yang C, LOHNER R, Lu H. An unstructured-grid based volume-of-fluid method for extreme wave and freely-floating structure interactions. Journal of Hydrodynamics, Ser B 2006;18(3):415–22.
[14] Yang C, Lohner R, Yim S. Development of a CFD simulation method for extreme wave and structure interactions. In: Proceedings of 24th int. Conference on offshore mech. and arctic eng. (OMAE2005), Halkidiki, Greece; 2005, p. 12–17.
[15] Chen G, Kharif C, Zaleski S, Li J. Two-dimensional Navier–Stokes simulation of breaking waves. Physics of Fluids 1999;11:121.
[16] He X, Chen S, Zhang R. A Lattice Boltzmann scheme for incompressible multiphase flow and its application in simulation of rayleigh-taylor instability. Journal of Computational Physics 1999;152(2):642–63.
[17] Hirt C, Nichols B. Volume of fluid (VOF) method for the dynamics of free boundaries. Journal of Computational Physics 1981;39(1):201–25.
[18] Draper S, Houlsby G, Oldfield M, Borthwick A. Modelling tidal energy extraction in a depth-averaged coastal domain. Renewable Power Generation, IET 2010;4(6):545–54.
[19] Harrison M, Batten W, Myers L, Bahaj A. Comparison between CFD simulations and experiments for predicting the far wake of horizontal axis tidal turbines. Renewable Power Generation, IET 2010;4(6):613–27.
[20] Myers L, Bahaj A. Experimental analysis of the flow field around horizontal axis tidal turbines by use of scale mesh disk rotor simulators. Ocean Engineering 2010;37(2–3):218–27.
[21] Sun X, Chick J, Bryden I. Laboratory-scale simulation of energy extraction from tidal currents. Renewable Energy 2008;33(6):1267–74.
[22] Sørensen J, Myken A. Unsteady actuator disc model for horizontal axis wind turbines. Journal of Wind Engineering and Industrial Aerodynamics 1992; 39(1–3):139–49.